# Optoelectronic control of single cells using organic photocapacitors

Marie Jakešová[1], Malin Silverå Ejneby[2], Vedran Đerek[1,3], Tony Schmidt[4], Maciej Gryszel[1,3], Johan Brask[2], Rainer Schindl[4], Daniel T. Simon[1], Magnus Berggren[1], Fredrik Elinder[2], Eric Daniel Głowacki[1,3]*

Optical control of the electrophysiology of single cells can be a powerful tool for biomedical research and technology. Here, we report organic electrolytic photocapacitors (OEPCs), devices that function as extracellular capacitive electrodes for stimulating cells. OEPCs consist of transparent conductor layers covered with a donor-acceptor bilayer of organic photoconductors. This device produces an open-circuit voltage in a physiological solution of 330 mV upon illumination using light in a tissue transparency window of 630 to 660 nm. We have performed electrophysiological recordings on *Xenopus laevis* oocytes, finding rapid (time constants, 50 μs to 5 ms) photoinduced transient changes in the range of 20 to 110 mV. We measure photoinduced opening of potassium channels, conclusively proving that the OEPC effectively depolarizes the cell membrane. Our results demonstrate that the OEPC can be a versatile nongenetic technique for optical manipulation of electrophysiology and currently represents one of the simplest and most stable and efficient optical stimulation solutions.

## INTRODUCTION

Devices based on extracellular stimulation of nerve tissue have been deployed therapeutically for many neurological conditions. The growing field of neural prosthetics includes cochlear and artificial retina implants as well as brain stimulation electrodes for the treatment of Parkinson's disease, depression, etc. (*1–3*). As an alternative to conventional metal or semiconductor electrodes, light stimulation offers the potential of wireless, temporally and locally specific, minimally invasive manipulation of electrophysiological processes. Optical control can be achieved directly by using near-infrared light (*4*), through genetic manipulation (i.e., optogenetics) (*5*), by delivery of photosensitive pharmaceuticals (*6*), or by an optoelectronic device (*7–9*). Examples of semiconducting films (*10–12*) and semiconducting nanoparticles (*13–17*) that are used to alter the electrophysiology of cells have been elaborated in considerable detail (*14, 18*). In these cases, either photothermal (*19*), photothermocapacitive (*4, 15*), or photofaradaic mechanisms (*13, 20, 21*) are implicated behind the observed (electro)physiological effects. The suitability of different stimulation mechanisms varies by desired application, and deeper mechanistic understanding is a topic of extensive current study (*22*). Nevertheless, there is a widely accepted consensus that, to achieve effective extracellular stimulation, a given charge threshold has to be delivered to the cell (*1, 23–25*). Unfortunately, the realization of optoelectronic devices generating large electrolytic charge densities remains elusive. We are motivated to find an effective optoelectronic method that relies on capacitive coupling at the single-cell level. Pioneering research on the biophysics of capacitive stimulation was done by Fromherz and coworkers (*26–28*). They showed the possibility of modulating cellular electrophysiology through externally electrically controlled thin-film dielectric capacitors. In view of their findings, we introduce a wireless light-sensitive

version: the organic electrolytic photocapacitor (OEPC). In our earlier work on organic semiconductor/single-cell interfaces, we were able to stimulate via a photothermal mechanism and did not reach the charging threshold for capacitive stimulation (*29*). Learning from these studies, we designed the first version of the OEPC and we were successful in demonstrating stimulation of blind chick retinas (*30*). We found reproducible action potential generation in retinal ganglion cells. Capacitive coupling was implicated as the mechanism in that work. In parallel, organic heterojunction blends capped with insulating layers have also been recently reported to deliver increased charge density (*31*). Here, we have taken a reductive approach to understand this mechanism conclusively and use this knowledge to optimize OEPC devices at the level of single cells.

Our motivation for using organic semiconductors to construct high-performance light-to-capacitive current transducers arises from several facts. Organic conjugated molecules are very efficient absorbers. Thus, our nanometrically thin devices absorb the same light that a 100× thicker silicon wafer would. Therefore, organic devices can be fabricated to be thin and less mechanically invasive. Furthermore, the stability and nontoxicity of many organic pigments are established (*32*). Last, the specific combination of materials used in this study, metal-free phthalocyanine ($H_2Pc$; p-type) and $N,N'$-dimethylperylene-3,4:9,10-tetracarboxylic diimide (PTCDI; n-type) (Fig. 1A), allows operation in the 630- to 660-nm tissue transparency window, thereby widening the scope from the artificial retina to other in vivo applications such as peripheral nerve stimulation. Here, we study the performance and stability of the next-generation OEPC (Fig. 1, A and B) as well as its capacitive coupling with single cells (Fig. 1, C and D). As a model single cell, we study *Xenopus laevis* oocytes. These cells are large (1 mm ø) and have a vitelline envelope surrounding the cell membrane, roughly 3 μm thick (*33*). The cleft between the membrane and the device surface is thus at least 3 μm. They are therefore a challenging system to demonstrate effective capacitive coupling, which mimics more closely realistic conditions for applied neurostimulation rather than cultured cells, which can form clefts of 20 to 50 nm with the semiconductor surface (*34*). In

[1]Laboratory of Organic Electronics, ITN Campus Norrköping, Linköping University, SE-60221 Norrköping, Sweden. [2]Department of Clinical and Experimental Medicine, Linköping University, SE-58185 Linköping, Sweden. [3]Wallenberg Centre for Molecular Medicine, Linköping University, SE-58185 Linköping, Sweden. [4]Gottfried Schatz Research Center, Medical University of Graz, A-8010 Graz, Austria.
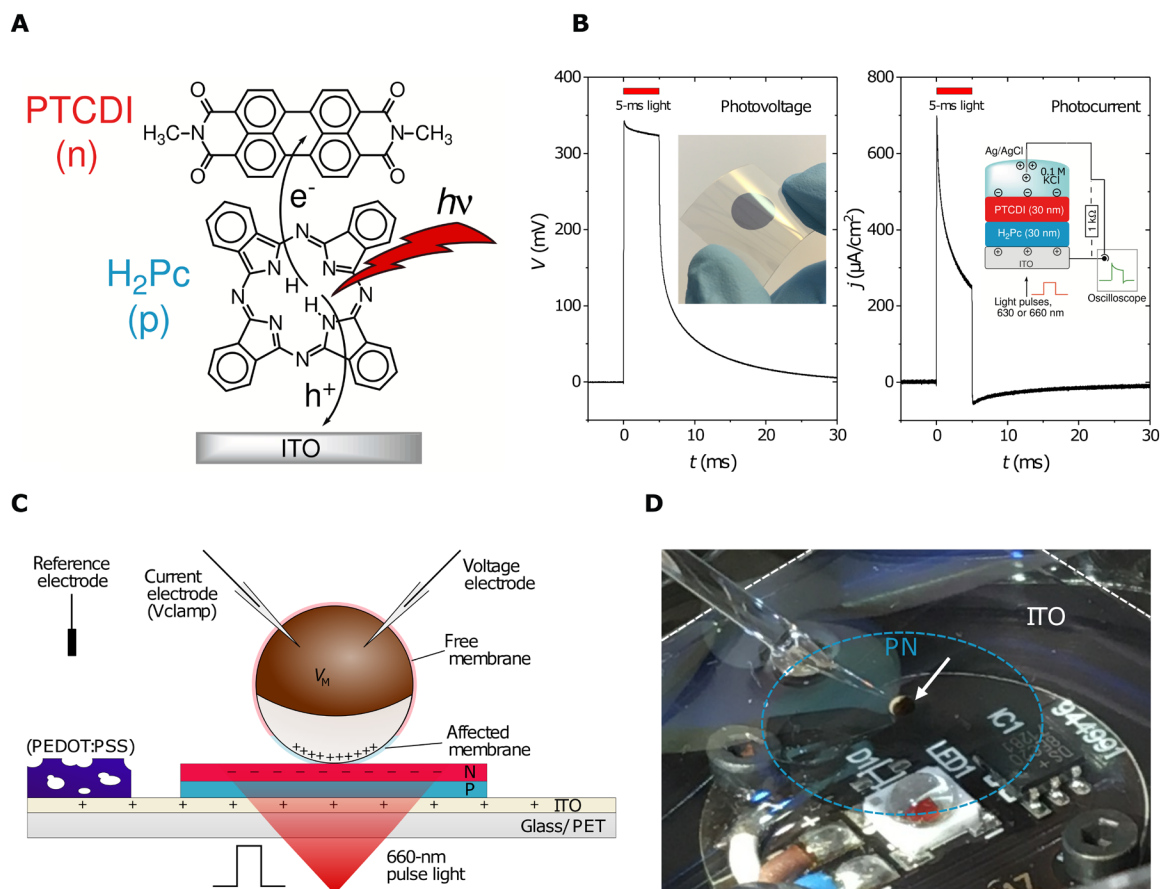*Corresponding author. Email: eric.glowacki@liu.se

**Fig. 1. The OEPC at the single-cell level.** (**A**) The mechanism of action of OEPC devices relies on photoinduced charge transfer between $H_2Pc$ (P-layer) as the electron donor and PTCDI (N-layer) as the electron acceptor. The conducting ITO layer plays a critical role in storing positive charge and serving as the return electrode in solution. (**B**) EPR measurements are used to characterize the photocharging dynamics of OEPC devices. Photovoltage is measured between the ITO and an Ag/AgCl reference electrode in solution, while the corresponding charging current is registered by measuring a voltage drop across a resistor. The insets show a photograph of an OEPC device on ITO-coated PET foil and a schematic of the EPR measurement configuration. (**C**) Cross-section of the OEPC device architecture, with an illustration of the capacitive coupling mechanism with an adjacent oocyte in the physiological electrolyte. Illustration shows the positive (+) and negative (−) charge density at the moment when photoinduced currents in the electrolyte have fully capacitively charged the oocyte. Single-cell electrophysiology experiments were carried out using one or two intracellular electrodes. The transient potential measured intracellularly by the voltage electrode is defined as $V_T$ in this paper. The actual membrane potential across a given region of the cell membrane is defined as $V_M$. The sign of the induced $V_M$ is represented in the illustration by the blue (positive) and red (negative) color of the cell membrane. In the vertical dimension, the thickness of the ITO/P/N structure is expanded for clarity. The thickness of the device layers is 110/30/30 nm, respectively. For voltage-clamp experiments where longer voltage transients are necessary, the capacitance of the device is boosted by adding a poly(3,4-ethylenedioxythiophene):polystyrene sulfonate (PEDOT:PSS) layer onto the ITO. (**D**) Photograph of the oocyte measurement setup with bottom LED illumination, with labeled PN region and ITO. The white arrow indicates the oocyte cell. Photo credit: E. D. Głowacki, Linköping University.

this work, we find that rapid and substantial changes of membrane potential are possible using the OEPC and unambiguously prove a capacitive coupling mechanism in achieving control of voltage-gated ion channels.

## RESULTS AND DISCUSSION
### Fabrication and stability of OEPCs
We introduced the concept of OEPCs in a previous study (*30*). The device comprises a conductive back electrode and a donor-acceptor junction of photosensitive organic semiconductor pigments, which, when immersed in electrolyte solution, form charged double layers upon illumination. We chose commercial indium tin oxide (ITO) on glass or poly(terephthalate) (PET) as a transparent conductor to serve as the bottom electrode in place of gold used in the original

study. ITO was favorable as it has a high overpotential for undesired faradaic processes (*35*), unlike gold, which can more easily catalyze various redox reactions. We found that OEPCs with gold photochemically produced reactive oxygen species, while ITO-based OEPCs did not (details in Supporting Note 1; fig. S1). The combination of donor-acceptor materials remained the same as previously described (i.e., 30 nm of $H_2Pc$ and 30 nm of PTCDI). The organic layers were obtained through sequential physical vapor deposition using a stencil mask. The performance of the devices was investigated by measuring the electrical photoresponse (EPR). A set of typical traces is shown in Fig. 1B, with the schematic of the setup in the inset. In short, the photovoltage response to pulsed red light (630 nm) is measured between the ITO back electrode and an Ag/AgCl counter electrode immersed in 0.1 M KCl, which is in contact with the organic pixel only, using an oscilloscope. The photocurrent is obtained

by measuring the voltage drop over a 1-kilohm resistor. This measurement provides information on the maximum achievable voltage (330 mV) and current density (0.6 to 0.7 mA/cm$^2$) of the device, as well as the associated charging/discharging dynamics. We used this technique to investigate the photostability of our devices as well as their endurance through sterilization. For in vitro and in vivo studies, sterilizability is an essential factor. The three sterilization procedures of choice were rinsing in 70% ethanol (EtOH), exposure to germicidal ultraviolet (UV) dose, or an autoclave cycle. The photostability test was accomplished by stressing the samples in the electrolyte with a constant pulsed illumination of 0.08 mW/mm$^2$ and 20-ms pulse with a 3.5% duty cycle (Fig. 2, A and B). All devices ($n = 20$, mean ± SD) produced a peak photovoltage of 331 ± 9 mV and a peak photocurrent density of 670 ± 38 μA/cm$^2$, as-fabricated when illuminated with a 630-nm red light-emitting diode (LED), giving an irradiance of 6 mW/mm$^2$. After sterilization ($n = 5$), the performance decreased by 5 to 10% for UV and EtOH treatments, while autoclaving resulted in a more substantial reduction. The parameters of UV- and EtOH-treated samples further declined after leaving the devices in an electrolyte (0.1 M KCl); however, the values were similar to those of unsterilized samples. To our surprise, the autoclaved samples recovered to higher performance than after fabrication. Afterward, the samples were exposed to continuous stress by pulsed illumination over 178 days (equivalent to around 27 million charge/discharge cycles). All samples remained functional, although performance declined slowly over time. Autoclaved samples overall kept the best performance. We hypothesized that the elevated performance was due to heat-induced recrystallization during the autoclave cycle (36). The autoclaved samples showed better-defined faceted crystals, providing evidence for heat-activated recrystallization

boosting performance (fig. S2). According to scanning electron microscopy (SEM) data, the nanoscale morphology difference between the as-fabricated samples (Fig. 2, C and D) and those exposed to stress over 178 days (Fig. 2E) evolves. All aged samples have a nanocrystalline morphology resembling autoclaved samples, implicating a surface recrystallization promoted by water. However, over longer periods of time (longer than 35 days), a process of progressive delamination of the organic layer at the edge was apparent (fig. S3). Erosion of the edge is observed, and redeposition of pieces of organic material both on the ITO layer and on top of the organic photoconductor nanocrystalline (PN) layer is clear. We hypothesize that adhesion of the PN layer to the conducting substrate over long periods of stress is the primary stability issue.

## Photoinduced membrane potential modulation

After obtaining stable and well-characterized devices, we moved on to study the light-induced effects on the electrophysiology of single cells. As a model, we used *X. laevis* oocytes. An advantage of this model is the large cell size and easy handling. In addition, oocytes offer easy exogenous ion channel expression as well as a low level of endogenous ion channels. In our initial exploration of the OEPC (30), we reported stimulation of neurons or retinal ganglion cells tens of micrometers in size, using OEPCs with diameters in the range of 50 to 2000 μm. For the relatively large oocytes (1 mm ∅), we use a correspondingly sized 12-mm ∅ organic pixel. First, we established the magnitude of transient voltage, $V_T$, induced in the oocytes. In these intracellular measurements, the OEPC is placed in an electrolyte bath, and the oocyte is positioned directly on top of the device, as shown in Fig. 1 (C and D). Unlike in the EPR measurements, the OEPC device is not wired in any way and is therefore
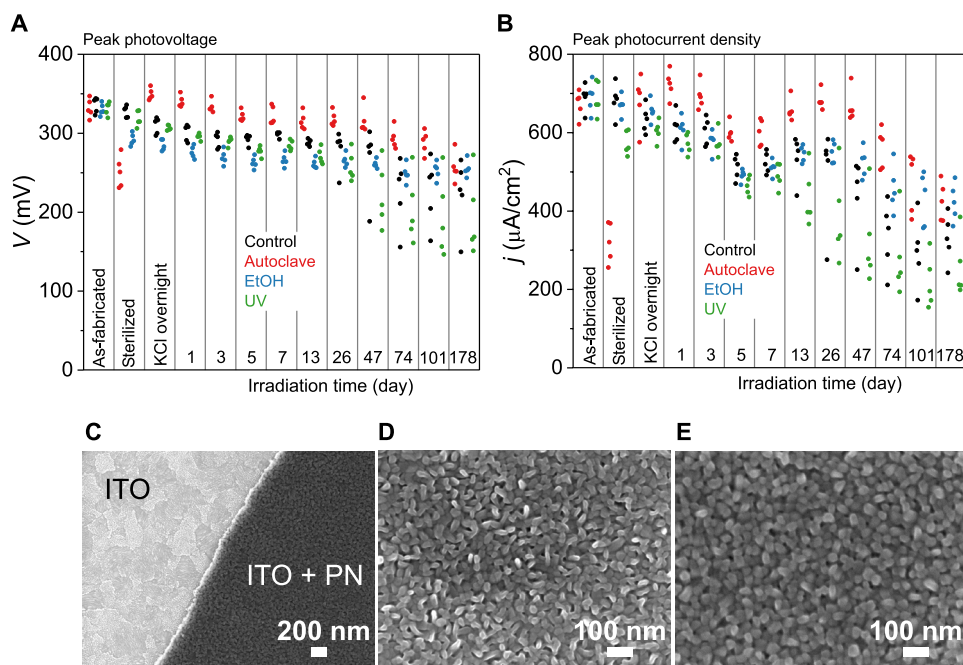


**Fig. 2. Stability and nanomorphology of OEPC devices.** (**A**) Peak photovoltage measured using the EPR of a series of devices subjected to a light stress test over 178 days. Three different sterilization conditions were applied, with autoclave yielding the most stable devices and UV resulting in faster performance decay. (**B**) Peak photocurrent of the same set of samples measured over the stress/stability test. (**C**) SEM micrograph of the edge of the organic PN layer on the ITO bottom electrode. This interface was stable for a month of stress but then began to experience delamination. (**D**) SEM of an as-fabricated organic PN layer and of a device (**E**) after 178 days of light pulse stress.

electrically floating. The recording is performed intracellularly, meaning that the voltage electrode is about 1 mm above the OEPC surface. The light pulse causes transient voltage peaks at the beginning and after the end of the pulse (10- and 1-ms pulses are shown in Fig. 3, A and B, respectively). The first negative peak had faster charging kinetics, while the second positive peak showed slower discharging corresponding to the discharging tail seen in the EPR measurement (Fig. 1B). The integrated area under both peaks was well balanced. The integration of the second peak gives 94.5 ± 1.4% of the value of the first peak. During the light pulse, the transient potential ($V_T$) typically returns to the resting membrane potential after ~3 ms. These positive-negative transient voltage peaks resemble transient potentials resulting from biphasic current pulses, which are typically used for electrical stimulation (30). We next studied the effect of light intensity on $V_T$. From Fig. 3C, it is evident that

with increasing light intensity, the magnitude of $V_T$ increases and begins to saturate at the highest intensity values. At the highest intensity of 6 mW/mm$^2$, the values were 110.1 ± 4.9 mV for the cathodic peak ($n$ = 12, means ± SEM). However, even the lowest probed intensity (0.3 mW/mm$^2$) delivered a $V_T$ of 23.9 ± 1.9 mV. For an excitable cell, this perturbation is above the threshold of what would be expected to elicit action potentials. To put the magnitude of these changes into context, we compare with recent studies of light-pulse irradiated organic donor-acceptor blends resulting in changes no higher than ±1 mV (18) or 80 mV, though this result was obtained with 72 mW/mm$^2$ (31). The efficiency of the capacitive coupling of our OEPC devices is therefore substantial.

When measured intracellularly in the oocyte, $V_T$ corresponds to the potential difference that the voltage electrode registers between the upper intracellular region of the oocyte and the distant reference
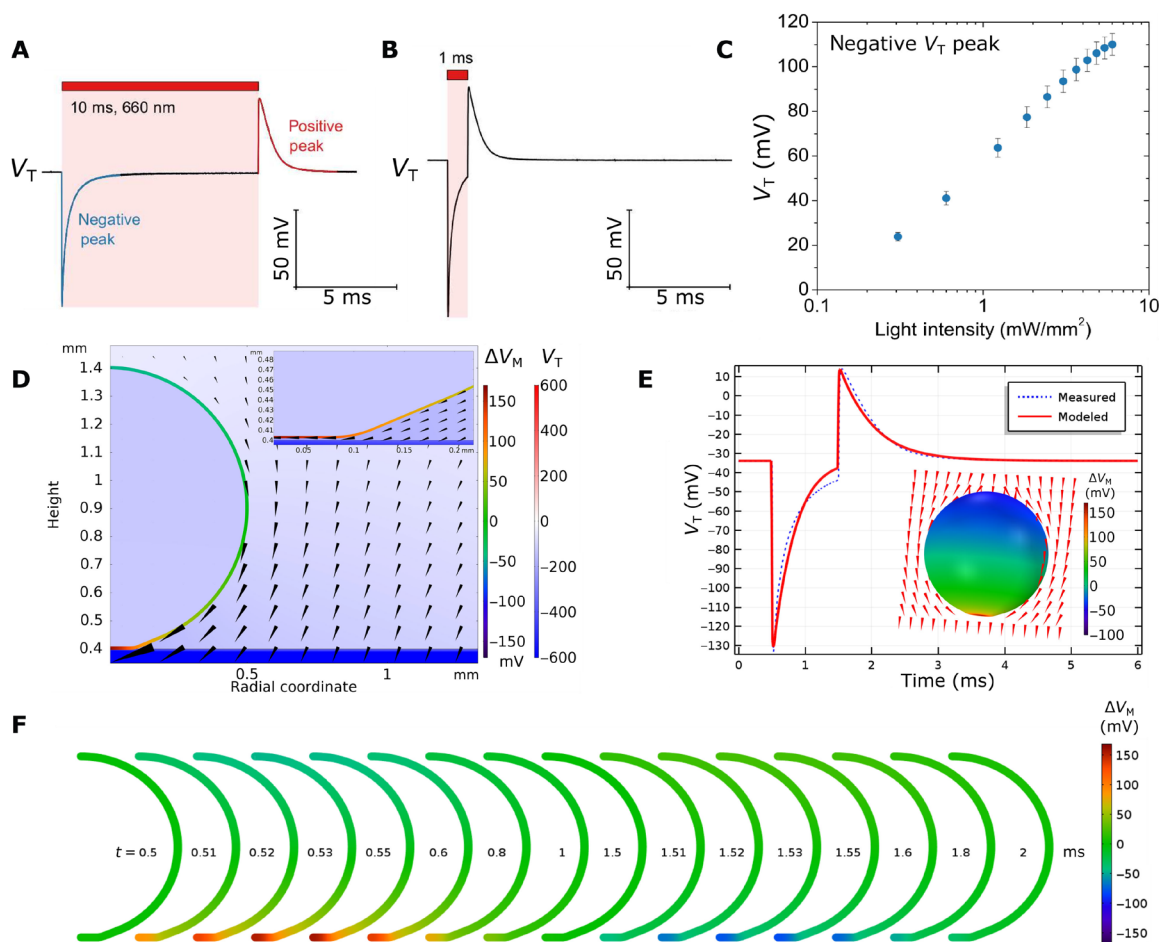


**Fig. 3. Photoinduced transient voltages and their effect on oocyte membrane potential. (A)** Photoinduced transient potential change measured intracellularly in an oocyte, showing the biphasic trace produced by a 10-ms illumination pulse. **(B)** $V_T$ for 1-ms pulse length. **(C)** Peak cathodic $V_T$ dependence on light intensity averages for 12 oocytes (pulse length, 250 μs). **(D)** Model of electrical potential during OEPC charging, showing both $V_T$ and arrows indicating ionic current direction and magnitude. The cell membrane is colored with a different color scale representing the calculated induced membrane potential, $\Delta V_M$. A resting membrane potential of −33 mV is assumed for all calculations. The bottom of the cell near the OEPC is depolarized, while the membrane on the top of the oocyte experiences a small hyperpolarization. A zoom of the cleft region showing the strongly depolarized region is given in the inset. A distance of 3 μm between the OEPC surface and the cell membrane is assumed for this calculation. Because of symmetry, only half of the oocyte is shown. **(E)** The calculated $V_T$ for a 1-ms pulse in the upper intracellular region of the oocyte (red trace) corresponds to the experimentally measured $V_T$ values (blue trace). The inset shows a three-dimensional (3D) projection of $V_M$ in different regions of the oocyte at the time point (50 μs after the light pulse is turned on) where the cathodic $V_T$ is maximum. The red region at the bottom of the oocyte represents the strongly depolarized part of the membrane near the OEPC surface. **(F)** 2D projection showing the time evolution of the induced membrane potential over the course of a 1-ms light pulse (turned on at $t$ = 0.5 ms, turned off at $t$ = 1.5 ms) and subsequent discharging (i.e., anodic peak).

electrode. However, this $V_T$ value is not equal in magnitude to the induced potential difference across the cell membrane, which would be felt by voltage-gated ion channels. To understand the magnitude of potential across different regions of the oocyte cell membrane, intra- versus extracellular, we applied a numerical model. Knowing the photocharging parameters of OEPCs from EPR measurements, electrolyte resistivity, and the areal capacitance of the oocyte ($1 \mu F/cm^2$), we constructed a numerical model to calculate the spatial and temporal evolution of $V_T$ and the corresponding photoinduced membrane potential ($V_M$). $V_M$, $V_T$, and spatial capacitive currents at the time of the maximum perturbation ($t = 0.55$ ms, 0.05 ms after the onset of light excitation) are plotted in Fig. 3D (see also figs. S4 and S5 for detailed conditions). In this model (details in Materials and Methods and Supporting Note 2), we assume a cleft distance of 3 μm, given mostly by the relatively thick vitelline envelope present on the oocyte and a flattened region at the bottom of the oocyte, where it rests on the OEPC surface. When we apply a light pulse, the OEPC charges and ionic displacement currents in solution cause transductive extracellular potentials (37), which last only when the OEPC device is charging or discharging. From this numerical simulation, it is apparent that only the bottom region of the oocyte, which we will refer to as the affected membrane, experiences a large depolarization, while the free membrane becomes slightly hyperpolarized. The numerical model reproduces a $V_T(t)$ trace resembling closely the experimentally measured one (Fig. 3E). Using this model, we can understand the relevant voltage polarity and magnitude affecting different regions of the oocyte membrane. The $V_M$ value for different phases of the photostimulation pulse is schematized in Fig. 3F and movie S1, showing the initial depolarization of the bottom part (affected membrane) of the oocyte when the light is turned on, followed by hyperpolarization of this region when the light is turned off. The validity of this model and electrophysiologically relevant photoinduced potential magnitudes will be evidenced experimentally in the following section concerning ion channel activation, where depolarization of the affected membrane is implicated.

Evaluating the possibility of photothermal effects is important. As a simple control, we fabricated dummy devices with an analogous absorber layer but that cannot electrically charge. For this purpose, we chose indigo as the organic pigment. The absorption spectrum of indigo overlaps that of $H_2Pc$ relatively well. Upon excitation, indigo undergoes rapid tautomerization and thus dissipates >99% of the energy in the form of heat (38). With the same light intensity settings as before, we could not see any difference between an oocyte on the indigo substrate and a blank petri dish. There are no photoinduced changes in the absence of a full OEPC device. The rate of heating is apparently not enough to elicit thermocapacitive changes. We hypothesize that in this case, where the absorbing surface is several micrometers away from the cell membrane, the transfer of thermal energy from the semiconductor surface to the cell is not efficient, thus minimizing the expectation of photothermal effects. Therefore, we propose that in the case of the OEPC devices at the applied time scales, the capacitive coupling model holds true and photothermal effects are negligible.

## Photoinduced ion channel opening
Once we established that the membrane potential could be perturbed by at least tens of millivolts, we went further to see whether we could use the OEPC device to evoke photoinduced activation of voltage-gated ion channels. We chose a well-understood wild-type (WT) Shaker $K_V$ channel expressed in *X. laevis* oocytes, and we measured the light-induced $K^+$ currents with the two-electrode voltage-clamp technique. These $K_V$ channels are opened by depolarizing potentials. The action of an additional capacitive electrode can be regarded as an "external voltage-clamp." If the proposed two-domain picture discussed above for capacitive coupling holds, we should expect photoinduced opening of the $K_V$ channels located in the affected region of the cell membrane adjacent to the OEPC. Because of the slow dynamics of the channel relative to the capacitive response of the cell to the applied voltage, one can expect steady-state ion channel currents only after several milliseconds. Because of this fact, our original OEPC device was not ideal for this experiment, because the $V_T$ perturbation decreases rapidly within milliseconds. To overcome this limitation, we tested two approaches. First, instead of a simple square pulse, we applied a light intensity ramp to prolong the charging of the OEPC. The other approach involved increasing the capacitance of the ITO back electrode, which allowed the OEPC system to accommodate more charge. We achieved this by partially coating the ITO with poly(3,4-ethylenedioxythiophene):polystyrene sulfonate (PEDOT:PSS) (as illustrated in Fig. 1C), a conducting polymer formulation known for its large electrolytic capacitance (39). Although the light intensity ramp made the residual $V_T$ at the end of the light pulse larger (fig. S6), the effects of PEDOT:PSS were superior. At the end of a 5-ms light pulse, the PEDOT:PSS-modified OEPC kept a $V_T$ value of up to 28 mV, while the unmodified sample decreased essentially to zero (Fig. 4A). The PEDOT:PSS-modified device has a larger time constant $\tau = RC$. Because the resistance has not changed, it is clear that the capacitance has increased and the OEPC can accommodate more charge over the whole course of the light pulse (Fig. 4A). Therefore, we continued all the voltage-clamp experiments with the PEDOT:PSS-modified samples only. As a point of reference, we studied the light pulse response to the voltage-clamp protocol on an uninjected oocyte with no exogenous ion channels present. Figure 4B shows that the light-induced capacitive response of the cell is independent of the applied command voltage. After expression of the Shaker $K_V$ channel, the photoresponse follows the channel behavior (Fig. 4C). Between applied −100 and −70 mV, when all the channels are closed, the light-induced response is the same, similar to an uninjected oocyte. However, by −50 mV, all the channels are still closed in the dark condition, but the light current is already nonzero. This change is attributed to the external OEPC-induced depolarizing field, causing channels in the affected membrane to open at more negative command voltages. These voltage-clamp traces are consistent with external capacitive stimulation achieved on $K_V1.3$ channels with electrically controlled capacitors (27). When one extracts the dark current before the pulse and the light current at the end of the pulse (Fig. 4C), the $I(V)$ characteristic can be constructed, and channel conductance, $G$, is calculated to give $G(V)$. A result of such treatment is given in Fig. 4D. The data show that the light pulses cause channel opening at up to 40 mV more negative command voltages. To confirm that all light-induced effects in this measurement originate from the flow of $K^+$, we applied the nonselective $K_V$ current blocker 4-aminopyridine (4-AP) to the WT Shaker $K_V$ channel. We observed inhibition of the light-induced effect in the $G(V)$ curves (Fig. 4D, green trace), with the raw voltage-clamp data resembling an uninjected oocyte. To further validate our proposed mechanism of photoinduced depolarization, we expressed a modified version of the Shaker $K_V$ channel with a $G(V)$ characteristic
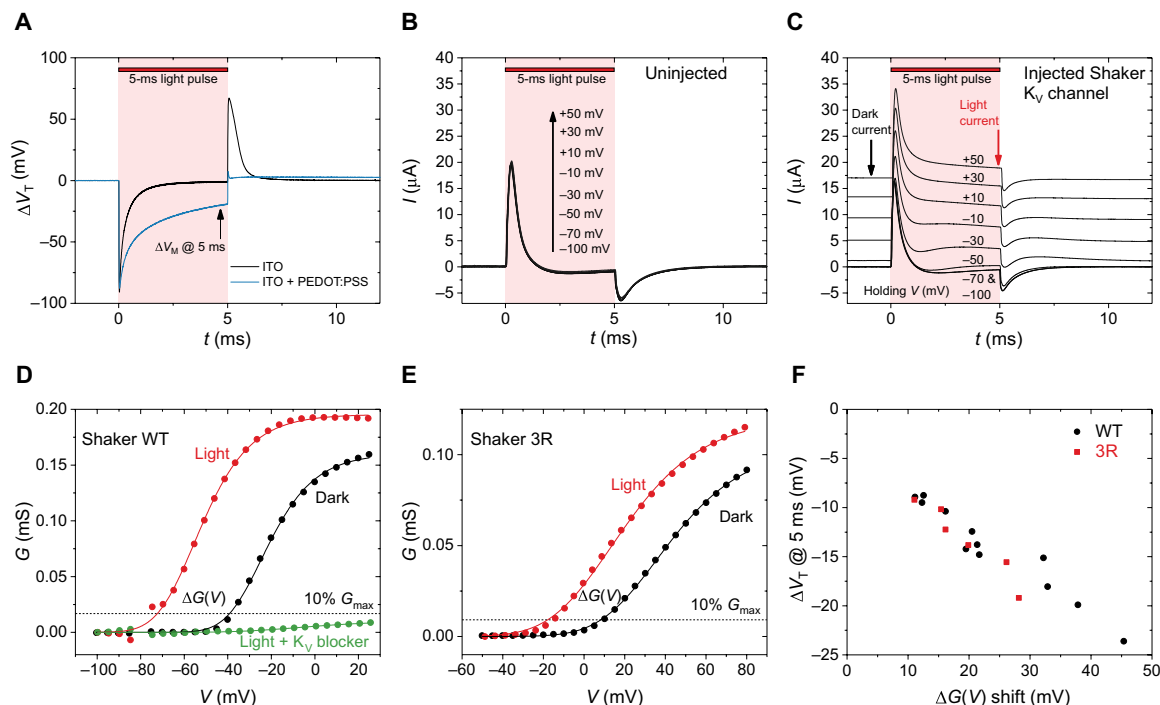
**Fig. 4. Photostimulation effects on $K_V$ Shaker-type channels in oocytes.** (**A**) Voltage measurements on uninjected oocytes using a 5-ms light pulse in the case where the bare ITO is the back electrode and the ITO is modified with PEDOT:PSS. Because of the higher capacitance given by PEDOT:PSS, the photocapacitive charging currents are larger and are exhibited over longer time, thus applying higher transductive extracellular potentials. Maximizing $V_T$ in a time scale of ≥2 ms is critical for observing effective stimulation of $K_V$ channels. We use $V_T$@5 ms here as a convenient reference. (**B**) Voltage-clamp measurements at various voltage steps in uninjected oocytes, showing the voltage-independent capacitive response of the cell to the light pulse. (**C**) Voltage-clamp measurements of an oocyte transfected with the Shaker $K_V$ channel, demonstrating the photoinduced increase in outward $K^+$ current. (**D**) $G(V)$ characteristic for WT Shaker $K_V$ channels, for dark conditions (black trace) and during the light pulse (red trace). The green trace is for measurement after addition of the $K_V$ channel blocker 4-AP. (**E**) $G(V)$ characteristics comparing dark conditions versus light pulses for 3R Shaker mutant channels. The onsets are shifted relative to WT. However, the photoinduced shift behavior is the same. (**F**) Correlation between the observed voltage shift in the light versus dark $G(V)$ and the transient voltage at the end of a 5-ms light pulse measured in the same cell. The higher transient voltage $V_T$ corresponds to greater observed shifts in the $G(V)$ characteristics.

shifted toward more positive potentials, the 3R Shaker $K_V$ channel (*40*). We saw the same photoinduced effect in the shifted 3R channel (Fig. 4E). To determine the relationship between the $G(V)$ curve shift and the performance of the OEPC in terms of the magnitude of photoinduced voltage change $V_T$, we constructed a correlation plot between the residual $V_T$ at the end of a 5-ms light pulse and the $\Delta V$ shift of the Shaker $G(V)$ curves (Fig. 4F). The data show different cell cohorts of the WT and mutant $K_V$ channels, and the light intensity applied was either 6 or 1.2 mW/mm². The correlation followed a clear trend, demonstrating that the $V_T$ perturbation observed corresponds to the shift in the opening of the ion channel. In summary, the OEPC can perform analogously to a capacitive electrode acting as an extracellular voltage source.

## CONCLUSIONS

In the present work, we have demonstrated efficient optical control of electrophysiology using a simple photocapacitive device based on organic semiconducting pigments, the OEPC. The motivation for developing OEPCs is to achieve a nongenetic, wireless, and minimally invasive analog to traditional electrodes, which are being used in fundamental research and medical applications treating neural dysfunction. In this work, we set out to understand the mechanism of action of OEPC at the single-cell level and see to what extent

capacitive coupling can be achieved. The OEPC can be regarded as an optoelectronic-to-ionic transducer. Photoexcitation of the donor-acceptor semiconductor junction produces electronic charges, which accumulate at the semiconductor/electrolyte and back electrode/electrolyte interfaces, producing oppositely charged electrolytic double layers. The electrolytic charging currents that result when short impulses of light are applied to the OEPC can be used to perturb the membrane potential in nearby cells. We found that capacitive coupling to oocytes was unexpectedly efficient, despite the relatively large effective cleft caused by the presence of the vitelline membrane on top of the oocyte's cellular membrane. The device can deliver voltage perturbations exceeding 100 mV intracellularly at the top of the oocyte, which is a distance of around 1 mm away from the OEPC surface. On the basis of numerical modeling, this perturbation translates to membrane potential changes on the level of tens to even over a hundred millivolts at different points of the cell. The values are well above levels necessary for action potential generation in excitable cells. This result validates why we were able to observe action potentials in the retinal ganglion cells we evaluated with the first version of the OEPC. One of the key findings of the study was the critical role of the back electrode not only in modulating the capacitance, and therefore dynamics, of the device but also as being the gatekeeper of photofaradaic processes. By boosting the capacitance of the back electrode through PEDOT:PSS modification, the

device *RC* time constant can be significantly increased and charging/discharging slowed down. The strongest evidence for the proposed mechanism of capacitive coupling is demonstrated by the opening of voltage-gated ion channels in a voltage-clamp measurement configuration, implicating effective optically induced membrane potential modulations of tens of millivolts. The OEPC here can be regarded as a light-activated external voltage-clamp electrode. This type of capacitive coupling experiment is rare and has been carried out in the case of electrically addressed capacitors only by Fromherz and coworkers in the past (*28*, *37*). The goal of achieving optoelectronic coupling to single cells using semiconductor materials and devices has garnered attention for nearly a decade (*9*, *13*, *14*). The experiments here constitute the first conclusive demonstration of successful and substantial capacitive coupling using an organic electronic device. Subsequent work will focus on optimizing parameters for eliciting action potentials in single cells, as well as transfer of the device on flexible implantable platforms for in vivo applications. Although the OEPC withstands sterilization and shows relative photostability, the performance, stability, and biocompatibility in vivo have to be established. Once that goal is reached, integration of the OEPC devices with sophisticated implantable platforms (*41*) enables many devices to treat neural disorders in a safe and less invasive manner.

## MATERIALS AND METHODS
### Materials and OEPC device fabrication
$H_2Pc$ (Alfa Aesar) and PTCDI (BASF) were used throughout this work. Both materials were purified three times by temperature gradient sublimation. ITO was used as a conducting layer on two different substrates: 125-µm-thick PET (Sigma-Aldrich) or 1.1-mm-thick borosilicate glass (Kintec). ITO substrates were cleaned by sequential sonication in acetone (only glass substrates), isopropanol, Hellmanex III detergent solution heated to 50°C, and deionized (DI) water. All samples were then exposed to UV/ozone treatment for 15 min and silanized in a vapor of *n*-octyltriethoxysilane (OTS) (TCI) at 90°C for 1 hour. Samples were sonicated in acetone (glass) or isopropanol (PET) and washed with water to remove any OTS multilayers. After OTS modification, substrates were moved to a multisource organic deposition system and pumped down to $1 \times 10^{-6}$ mbar. $H_2Pc$ was evaporated at a rate of 1 to 2 Å/s to a thickness of 30 nm, and PTCDI was evaporated at a rate of 2 to 5 Å/s to a thickness of 30 nm. Rate control was verified using a quartz crystal microbalance, with previous thickness calibration using a Dektak contact profilometer cross-checked with absorbance measurements, which allowed comparison to optical density values for thin films reported in the literature. The indigo samples were prepared similarly, except the thickness of the absorber was 60 nm to compensate for the lower absorption coefficient. Patterning of the organic semiconductor layer was done using stencil shadow masking. For OEPC devices with an additional PEDOT:PSS layer added to the ITO back contact, the procedure was modified slightly: During the OTS vapor-phase deposition, the edges of the ITO were protected with a stencil tape. This effectively masked the OTS deposition and left the protected areas hydrophilic. The sample was then spin-coated with a commercial PEDOT:PSS formulation (PH1000, Heraeus GmbH). The PH1000 mixture was modified by adding 1% (by volume) dimethyl sulfoxide (DMSO) and 1 volume % (3-glycidyloxypropyl)trimethoxysilane (GOPS). GOPS was added to provide good adhesion to the ITO, while DMSO was an additive that increased the PEDOT:PSS conduc-

tivity. The modified PH1000 mixture was spin-coated from freshly made solutions at 1500 rpm for 30 s, following a 2-s spreading step at 800 rpm. Coated samples were baked on a hotplate at 120°C for 10 min. PEDOT:PSS was found to stick only to the hydrophilic edges and did not deposit on the OTS modified area in the center of the substrate. The SEM images were obtained on a ZEISS Sigma 500 FE-SEM using an in-lens secondary electron detector and with an acceleration voltage of 3 kV.

### EPR measurements
EPR data were collected using a high-resolution 15-bit two-channel PicoScope 5243B oscilloscope. Measurements were conducted inside a dark faraday cage. Light excitation was achieved with a 630-nm red LED placed behind a transparent glass window below the sample stage, giving an irradiance of 6 mW/mm$^2$ at the sample position on the stage. Contact to the transparent conductor back electrode of the devices was established with a needle probe, while the electrolyte contact was achieved with an AgCl-coated silver wire placed in a syringe containing 0.1 M KCl electrolyte. The electrode-containing syringe was positioned above the device using a holder with the screw-controllable *z* axis. The level of the electrolyte in the electrode-containing syringe was controlled manually by adjusting the pressure with an empty syringe connected by flexible tubing to the electrode-containing syringe. In this way, the top electrolyte contact to the devices was accomplished without mechanical contact by a drop of the electrolyte from the syringe. The EPR voltage measurements were taken directly with an oscilloscope, while the current measurements were obtained by measuring the voltage drop over a 1-kilohm resistor shorting the electrolyte contact and the back contact to the devices or by using a low-impedance (50-ohm) low-noise current amplifier (FEMTO DLPCA-200). The devices (15 mm by 15 mm ITO, 8 Ø mm organic pixel) were sterilized in three different ways: They were either washed three times in 70% EtOH for 5 s with rinses of DI water in between, exposed to UV irradiation (8000 µW s/cm$^2$), or autoclaved at 121°C for 20 min (Tuttnauer, Elara 9i). The samples were measured 2 hours after the sterilization process. The irradiation stress was performed by exposing the OEPCs immersed in 0.1 M KCl to a high-density LED light source (626 nm, 0.08 mW/mm$^2$) pulsed at 20 ms with a 550-ms interval. Before measurement, the samples were washed with DI water and dried under a stream of nitrogen. Samples measured for 178 days were allowed to rest for 4 hours before the final measurement.

### Electrophysiology with *X. laevis* oocytes
The Shaker H4 channel (*42*) containing Δ(6–46) deletion to suppress fast inactivation (*43*), referred to as the WT Shaker K$_V$ channel, and its modification with two introduced arginine residues (M356R, A359R, R362), referred to as the 3R Shaker K$_V$ channel (*40*), were used throughout this study. Mutagenesis, oocyte preparation, storage, complementary RNA (cRNA) synthesis, and injection followed the procedures described previously (*44*, *45*). Animal experiments were approved by the local Animal Care and Use Committee at Linköping University. All chemicals were purchased from Sigma-Aldrich if not stated otherwise. Experiments were performed with a GeneClamp 500B amplifier (Axon Instruments) and pClamp 10 software (Molecular Devices) and were digitized with a Digidata 1440A converter (Molecular Devices) at 4 µs per point. For the two-electrode voltage-clamp data, the amplifier's leak compensation was used, and the currents were low pass–filtered at 10 kHz. All experiments

were done at room temperature (20° to 23°C). The extracellular solution was composed of 88 mM NaCl, 1 mM KCl, 15 mM Hepes, 0.4 mM CaCl$_2$, and 0.8 mM MgCl$_2$ with pH adjusted to 7.4 with NaOH. The intracellular electrodes were prepared from borosilicate glass capillaries (World Precision Instruments) using an electrode puller (Narishige) to obtain a resistance of 0.5 to 2.0 megohms when filled with 3 M KCl. The measurement chamber was a 50-mm petri dish, with the OEPC device (25.4 by 25.4 mm ITO, 13 mm Ø organic pixel) placed centrally on a mounted LED (660 nm, 0.06 to 6 mW/mm$^2$, operated with DC2200 High-Power LED Driver, Thorlabs). The oocyte was positioned in the center of the organic pixel. For the $V_T$ experiment, the voltage electrode was inserted into an oocyte (voltage follower amplifier), and the reference electrode was placed in the bath next to the OEPC device. The changes in potential upon pulsed light were measured. For the two-electrode voltage-clamp experiments, an additional electrode was used. The holding voltage was set to −100 mV (WT Shaker K$_V$) or −70 mV (3R Shaker K$_V$), and steady-state currents were measured between −100 and +50 mV for the WT Shaker K$_V$ channel and between −70 and +80 mV for the 3R Shaker K$_V$ channel with 5-mV steps, each for 150 ms. For the light experiments, a 3- to 10-ms light pulse was applied at 100 ms of the voltage step. All the shown voltage-clamp experiments were performed with the PEDOT:PSS-modified OEPCs, which were soaked in an electrolyte for at least 1 day before measurements. The blocking experiments were measured by adding 10 mM 4-AP (Alomone Labs) into the bath solution, yielding a final concentration of ~2 mM. The channel $G(V)$ curves were constructed according to $G_K(V) = I_K/(V − V_{rev})$, where $I_K$ is the steady-state current before the light pulse (dark) and 100 μs before the end of the 5-ms light pulse (light). The light ionic current was corrected for the light-induced capacitive current by subtracting $I_K$ at the most negative applied potential, where all ion channels are closed, $V$ is the absolute membrane potential, and $V_{rev}$ is the reversal potential for the K channel, here set to −80 mV. The light-induced shift in the $G(V)$ curve was estimated at 10% level of the maximum dark conductance. For this purpose, $G(V)$ was fitted with a Boltzmann equation raised to the fourth power $G(V) = A/(1 + \exp((V_{50} − V)/s))^4$, where $A$ is the amplitude, $V_{50}$ is the midpoint, and $s$ is the slope factor, as described previously (44).

## Numerical modeling

The time-dependent electrical behavior of the photocapacitor/ electrolyte/oocyte system was numerically modeled in a pseudo– three-dimensional (3D) axiosymmetric geometry using a finite element analysis software (COMSOL Multyphysics version 5.3a, COMSOL Inc.). The effect of the photocapacitive excitation on the system was represented by a 4-mm-diameter conductive disc with infinite contact resistivity to replicate the nonfaradaic nature of the excitation. The disc was put in an electrically conductive medium (a circular right cylinder 5 mm in diameter and 3.5 mm in height, electric conductivity of 1.25 S/m, grounded on the top and the sides) representing the electrolyte used in the oocyte experiments. The oocyte cell was modeled as a 1-mm-diameter truncated sphere, with a 200-μm-diameter truncated flat zone at the bottom, representing the contact area with the photocapacitor. The model cell was placed at a distance of 3 μm from the model photocapacitor, a distance that we believe accurately represents the cleft width in the modeled system. The model cell was given an infinite surface resistance, representing the lack of endogenous ion channels, a surface capacitance of 1 μF/cm$^2$, and a resting potential of −34 mV. A 1-ms

constant voltage pulse starting at 0.5 ms was applied to the disc, resulting in capacitive spatial currents in the electrolyte and the oocyte. To faithfully model the charging and discharging dynamics of the system due to the differing properties of the photocapacitor in the light versus dark phase, the disc bulk conductivity and contact capacitance were fitted separately during the light excitation phase and the "dark" part of the time-dependent study. The disc bulk conductivity, surface capacitance, and excitation voltage were initially set to match the measured injected current density (200 to 600 μA/cm$^2$) by the photocapacitor under the light intensity used in the experiment. The photocapacitor/electrolyte interface capacitance was set to the value (3 to 4 μF/cm$^2$) previously determined by electrochemical impedance spectroscopy (30). The parameters were further refined to match as closely as possible the measured intracellular voltage transient $V_T$ from the inside of the oocyte (Fig. 3, A and E). The response of the modeled system (capacitive currents, resulting transient voltages, and changes in the cell membrane potential) to the voltage pulse representing the light excitation are shown in Fig. 3 and movie S1. Further details can be found in Supporting Note 2.

## SUPPLEMENTARY MATERIALS

Supporting Note 1. Photofaradaic reactions: Quantification of H$_2$O$_2$ production.
Supporting Note 2. Numerical modeling of the OEPC/oocyte interface.
Table S1. Results of H$_2$O$_2$ photogeneration.
Fig. S1. Illustration of photocapacitive versus photofaradaic behavior in OEPCs.
Fig. S2. SEM micrographs comparing control samples of ITO/H$_2$Pc/PTCDI.
Fig. S3. SEM micrographs of samples subjected to 178 days of light pulse stress.
Fig. S4. 2D representation of the electrolyte/oocyte/photocapacitor system.
Fig. S5. A 3D representation of the oocyte/photocapacitor model.
Fig. S6. Comparison of voltage transients in the case of light intensity ramps with a standard square light pulse.
Movie S1. Animation of evolution of transient potentials and membrane potentials during a 1-ms illumination pulse for an oocyte on top of an OEPC.

## REFERENCES AND NOTES

1. S. F. Cogan, Neural stimulation and recording electrodes. *Annu. Rev. Biomed. Eng.* **10**, 275–309 (2008).
2. N. Pour Aryan, H. Kaim, A. Rothermel, *Stimulation and Recording Electrodes for Neural Prostheses* (Springer, 2015).
3. T. Someya, Z. Bao, G. G. Malliaras, The rise of plastic bioelectronics. *Nature* **540**, 379–385 (2016).
4. M. G. Shapiro, K. Homma, S. Villarreal, C.-P. Richter, F. Bezanilla, Infrared light excites cells by changing their electrical capacitance. *Nat. Commun.* **3**, 736 (2012).
5. M. Scanziani, M. Häusser, Electrophysiology in the age of light. *Nature* **461**, 930–939 (2009).
6. W. A. Velema, W. Szymanski, B. L. Feringa, Photopharmacology: Beyond proof of principle. *J. Am. Chem. Soc.* **136**, 2178–2191 (2014).
7. D. Palanker, A. Vankov, P. Huie, S. Baccus, Design of a high-resolution optoelectronic retinal prosthesis. *J. Neural Eng.* **2**, S105–S120 (2005).
8. K. Mathieson, J. Loudin, G. Goetz, P. Huie, L. Wang, T. I. Kamins, L. Galambos, R. Smith, J. S. Harris, A. Sher, D. Palanker, Photovoltaic retinal prosthesis with high pixel density. *Nat. Photonics* **6**, 391–397 (2012).
9. F. Benfenati, G. Lanzani, New technologies for developing second generation retinal prostheses. *Lab. Anim.* **47**, 71–75 (2018).
10. D. Ghezzi, M. R. Antognazza, R. Maccarone, S. Bellani, E. Lanzarini, N. Martino, M. Mete, G. Pertile, S. Bisti, G. Lanzani, F. Benfenati, A polymer optoelectronic interface restores light sensitivity in blind rat retinas. *Nat. Photonics* **7**, 400–406 (2013).
11. V. Gautam, D. Rand, Y. Hanein, K. S. Narayan, A polymer optoelectronic interface provides visual cues to a blind retina. *Adv. Mater.* **26**, 1751–1756 (2014).
12. L. Ferlauto, M. J. I. Airaghi Leccardi, N. A. L. Chenais, S. C. A. Gilliéron, P. Vagni, M. Bevilacqua, T. J. Wolfensberger, K. Sivula, D. Ghezzi, Design and validation of a foldable and photovoltaic wide-field epiretinal prosthesis. *Nat. Commun.* **9**, 992 (2018).
13. T. C. Pappas, W. M. S. Wickramanyake, E. Jan, M. Motamedi, M. Brodwick, N. A. Kotov, Nanoscale engineering of a cellular interface with semiconductor nanoparticle films for photoelectric stimulation of neurons. *Nano Lett.* **7**, 513–519 (2007).

14. L. Bareket-Keren, Y. Hanein, Novel interfaces for light directed neuronal stimulation: Advances and challenges. *Int. J. Nanomedicine* **9**, 65–83 (2014).

15. Y. Jiang, J. L. Carvalho-de-Souza, R. C. S. Wong, Z. Luo, D. Isheim, X. Zuo, A. W. Nicholls, I. W. Jung, J. Yue, D.-J. Liu, Y. Wang, V. de Andrade, X. Xiao, L. Navrazhnykh, D. E. Weiss, X. Wu, D. N. Seidman, F. Bezanilla, B. Tian, Heterogeneous silicon mesostructures for lipid-supported bioelectric interfaces. *Nat. Mater.* **15**, 1023–1030 (2016).

16. R. Parameswaran, B. Tian, Rational design of semiconductor nanostructures for functional subcellular interfaces. *Acc. Chem. Res.* **51**, 1014–1022 (2018).

17. M. Zangoli, F. di Maria, E. Zucchetti, C. Bossio, M. R. Antognazza, G. Lanzani, R. Mazzaro, F. Corticelli, M. Baroncini, G. Barbarella, Engineering thiophene-based nanoparticles to induce phototransduction in live cells under illumination. *Nanoscale* **9**, 9202–9209 (2017).

18. O. S. Abdullaeva, M. Schulz, F. Balzer, J. Parisi, A. Lützen, K. Dedek, M. Schiek, Photoelectrical stimulation of neuronal cells by an organic semiconductor–electrolyte interface. *Langmuir* **32**, 8533–8542 (2016).

19. N. Martino, P. Feyen, M. Porro, C. Bossio, E. Zucchetti, D. Ghezzi, F. Benfenati, G. Lanzani, M. R. Antognazza, Photothermal cellular stimulation in functional bio-polymer interfaces. *Sci. Rep.* **5**, 8911 (2015).

20. C. Tortiglione, M. R. Antognazza, A. Tino, C. Bossio, V. Marchesano, A. Bauduin, M. Zangoli, S. V. Morata, G. Lanzani, Semiconducting polymers are light nanotransducers in eyeless animals. *Sci. Adv.* **3**, e1601699 (2017).

21. R. Parameswaran, J. L. Carvalho-de-Souza, Y. Jiang, M. J. Burke, J. F. Zimmerman, K. Koehler, A. W. Phillips, J. Yi, E. J. Adams, F. Bezanilla, B. Tian, Photoelectrochemical modulation of neuronal activity with free-standing coaxial silicon nanowires. *Nat. Nanotechnol.* **13**, 260–266 (2018).

22. Y. Jiang, X. Li, B. Liu, J. Yi, Y. Fang, F. Shi, X. Gao, E. Sudzilovsky, R. Parameswaran, K. Koehler, V. Nair, J. Yue, K. Guo, Y. Fang, H.-M. Tsai, G. Freyermuth, R. C. S. Wong, C.-M. Kao, C.-T. Chen, A. W. Nicholls, X. Wu, G. M. G. Shepherd, B. Tian, Rational design of silicon structures for optically controlled multiscale biointerfaces. *Nat. Biomed. Eng.* **2**, 508–521 (2018).

23. S. B. Brummer, L. S. Robblee, F. T. Hambrecht, Criteria for selecting electrodes for electrical stimulation: Theoretical and practical considerations. *Ann. N. Y. Acad. Sci.* **405**, 159–171 (1983).

24. D. R. Merrill, M. Bikson, J. G. R. Jefferys, Electrical stimulation of excitable tissue: Design of efficacious and safe protocols. *J. Neurosci. Methods* **141**, 171–198 (2005).

25. E. S. Krames, P. H. Peckham, A. R. Rezai, *Neuromodulation* (Academic Press, 2009).

26. I. Schoen, P. Fromherz, Activation of Na$^+$ channels in cell membrane by capacitive stimulation with silicon chip. *Appl. Phys. Lett.* **87**, 193901 (2005).

27. M. H. Ulbrich, P. Fromherz, Opening of K$^+$ channels by capacitive stimulation from silicon chip. *Appl. Phys. A* **81**, 887–891 (2005).

28. I. Schoen, P. Fromherz, The mechanism of extracellular stimulation of nerve cells on an electrolyte-oxide-semiconductor capacitor. *Biophys. J.* **92**, 1096–1111 (2007).

29. M. Sytnyk, M. Jakešová, M. Litviňuková, O. Mashkov, D. Kriegner, J. Stangl, J. Nebesářová, F. W. Fecher, W. Schöfberger, N. S. Sariciftci, R. Schindl, W. Heiss, E. D. Głowacki, Cellular interfaces with hydrogen-bonded organic semiconductor hierarchical nanocrystals. *Nat. Commun.* **8**, 91 (2017).

30. D. Rand, M. Jakešová, G. Lubin, I. Vėbraitė, M. David-Pur, V. Đerek, T. Cramer, N. S. Sariciftci, Y. Hanein, E. D. Głowacki, Direct electrical neurostimulation with organic pigment photocapacitors. *Adv. Mater.* **30**, 1707292 (2018).

31. O. S. Abdullaeva, F. Balzer, M. Schulz, J. Parisi, A. Lützen, K. Dedek, M. Schiek, Organic photovoltaic sensors for photocapacitive stimulation of voltage-gated ion channels in neuroblastoma cells. *Adv. Funct. Mater.* **2018**, 1805177 (2018).

32. K. Hunger, Toxicology and toxicological testing of colorants. *Rev. Prog. Color. Relat. Top.* **35**, 76–89 (2005).

33. V. Kiessling, S. Vassanelli, Potassium channel gating in adhesion: From an oocyte-silicon to a neuron-astrocyte adhesion contact. *Eur. Biophys. J.* **34**, 113–126 (2005).

34. F. Santoro, S. Dasgupta, J. Schnitker, T. Auth, E. Neumann, G. Panaitov, G. Gompper, A. Offenhäusser, Interfacing electrogenic cells with 3D nanoelectrodes: Position, shape, and size matter. *ACS Nano* **8**, 6713–6723 (2014).

35. J. D. Benck, B. A. Pinaud, Y. Gorlin, T. F. Jaramillo, Substrate selection for fundamental studies of electrocatalysts and photoelectrodes: Inert potential windows in acidic, neutral, and basic electrolyte. *PLOS ONE* **9**, e107942 (2014).

36. M. Warczak, M. Gryszel, M. Jakešová, V. Đerek, E. D. Głowacki, Organic semiconductor perylenetetracarboxylic diimide (PTCDI) electrodes for electrocatalytic reduction of oxygen to hydrogen peroxide. *Chem. Commun.* **54**, 1960–1963 (2018).

37. I. Willner, E. Katz, *Bioelectronics* (Wiley-VCH, Weinheim, 2005).

38. E. D. Głowacki, G. Voss, N. S. Sariciftci, 25th anniversary article: Progress in chemistry and applications of functional indigos for organic electronics. *Adv. Mater.* **25**, 6783–6800 (2013).

39. C. M. Proctor, J. Rivnay, G. G. Malliaras, Understanding volumetric capacitance in conducting polymers. *J. Polym. Sci. Part B Polym. Phys.* **54**, 1433–1436 (2016).

40. N. E. Ottosson, S. I. Liin, F. Elinder, Drug-induced ion channel opening tuned by the voltage sensor charge profile. *J. Gen. Physiol.* **143**, 173–182 (2014).

41. D. Khodagholy, J. N. Gelinas, Z. Zhao, M. Yeh, M. Long, J. D. Greenlee, W. Doyle, O. Devinsky, G. Buzsáki, Organic electronics for high-resolution electrocorticography of the human brain. *Sci. Adv.* **2**, e1601027 (2016).

42. A. Kamb, L. E. Iverson, M. A. Tanouye, Molecular characterization of Shaker, a Drosophila gene that encodes a potassium channel. *Cell* **50**, 405–413 (1987).

43. T. Hoshi, W. N. Zagotta, R. W. Aldrich, Biophysical and molecular mechanisms of shaker potassium channel inactivation. *Science* **250**, 533–538 (1990).

44. S. I. Börjesson, T. Parkkari, S. Hammarström, F. Elinder, Electrostatic tuning of cellular excitability. *Biophys. J.* **98**, 396–403 (2010).

45. N. E. Ottosson, X. Wu, A. Nolting, U. Karlsson, P.-E. Lund, K. Ruda, S. Svensson, P. Konradsson, F. Elinder, Resin-acid derivatives as potent electrostatic openers of voltage-gated K channels and suppressors of neuronal excitability. *Sci. Rep.* **5**, 13278 (2015).